Technical University of Denmark

DTU

Size scale dependence of compressive instabilities in layered composites in the presence of stress gradients

Poulios, Konstantinos; Niordson, Christian Frithiof

[Link back to DTU Orbit]

DTU Library
Technical Information Center of Denmark

Size scale dependence of compressive instabilities in layered composites in the presence of stress gradients

You may also be interested in:

Size scale dependence of compressive instabilities in layered composites in the presence of stress gradients

K Poulios and C F Niordson

Department of Mechanical Engineering, Solid Mechanics, Technical University of Denmark, Nils Koppels Allé, DK-2800 Kgs. Lyngby, Denmark

E-mail: `kopo@mek.dtu.dk`

Abstract.   The compressive strength of unidirectionally or layer-wise reinforced composite materials in direction parallel to their reinforcement is limited by micro-buckling instabilities. Although the inherent compressive strength of a given material micro-structure can easily be determined by assessing its stability under a uniform compressive load, this is often not sufficient for predicting failure initiation within a larger structure. In cases, where the composite material micro-structure is locally subjected to strongly non-uniform loadings, compressive instabilities depend not only on the maximum compressive stress but also on spatial stress or strain gradients, rendering failure initiation size scale dependent. The present work demonstrates and investigates the aforementioned effect through numerical simulations of periodically layered structures with notches and holes under bending and compressive loads, respectively. The presented results emphasize the importance of the reinforcing layer thickness on the load carrying capacity of the investigated structures, at a constant volumetric fraction of the reinforcement. The observed strengthening at higher values of the relative layer thickness is attributed to the bending stiffness of the reinforcing layers.

1. Introduction

The load carrying capacity of structures made of strongly anisotropic composite materials is often determined by failure under compressive loads parallel to the reinforcement. Due to its vast practical importance, this kind of failure has been subject of extensive research including both experimental and numerical investigations. Two major effects related to compressive failure of unidirectionally reinforced composites are micro-buckling and formation of kink-bands, [1].

Historically, significant research effort went into understanding the early observed discrepancies between the predictions of the classical limit of Rosen, [2], for elastic micro-buckling and the significantly lower experimentally determined compressive strengths. Argon suggested a different compressive instability limit, based on an assumed local misalignment of the reinforcement and plastic yielding of the matrix material, [3]. Later, Budiansky proposed a combination of Rosen's and Argon's limits into a single expression, [4], and Budiansky and Fleck extended this limit to the case of a matrix material with isotropic hardening of Ramberg-Osgood type, [5].

These very fundamental investigations, determined the inherent compressive strength of a considered composite under a spatially constant and longitudinal compressive stress. In a real structure though, the material micro-structure is generally subjected to arbitrary stress states, possibly including significant spatial gradients. The load carrying capacity of a structure is

then determined as a combination of the material micro-structure properties and the macro-structure design and loads. Waas proposed a semi-analytical model for predicting elastic micro-buckling initiation close to a free surface and in the presence of stress gradients, [6]. Fleck and Shu developed a numerical model based on a homogenized representation of the material micro-structure for studying elasto-plastic micro-buckling initiation for different kinds of fiber misalignments, [7] . Kyriakides et al. compared numerical and experimental results of kink-band formation, based on a finite-element model with explicitly discretized micro-structure, [8]. Following the same approach, Wind et al. determined the bending load capacity of a longitudinally reinforced V-notched beam both experimentally and numerically, [9].

Based on numerical examples, the present work demonstrates that at the presence of stress gradients, prediction of compressive failure initiation is not trivial and not easy to capture by analytic models.

2. Numerical Model

This section provides a brief summary of the homogenized finite-element model, introduced in [10], which is used for all simulations, presented in the next section. The main characteristic of the model, is that it involves three unknown fields to solve for: the displacements field $\boldsymbol{u}$, the internal kinematic variable field $\boldsymbol{d}$ and the plastic multiplier field ξ_m. The physical meaning of the vector variable $\boldsymbol{d}$ is illustrated in figure 1, which also defines the unit vectors $\boldsymbol{T}$ and $\boldsymbol{N}$, respectively tangential and normal to the fiber direction.
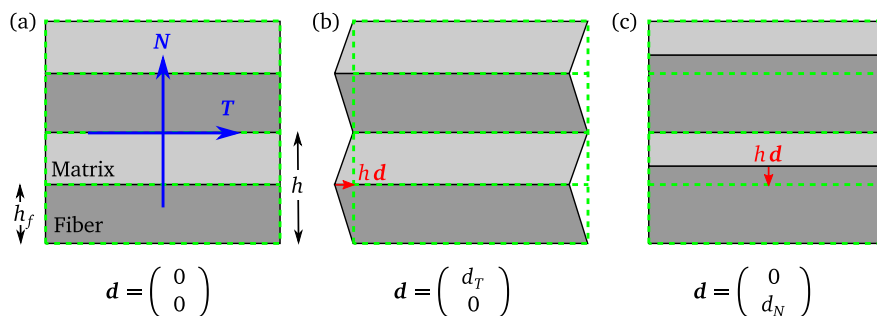
Figure 1. Undeformed and arbitrary deformed configurations of the micro-structure.

A kinematic analysis of the considered micro-structure leads to average deformation gradient tensors for the fiber and the matrix materials respectively defined as

$$\boldsymbol{F}_f = \boldsymbol{I} + \nabla \boldsymbol{u} - \frac{1}{c_f} \boldsymbol{d} \boldsymbol{N}^T \tag{1}$$

and

$$\boldsymbol{F}_m = \boldsymbol{I} + \nabla \boldsymbol{u} + \frac{1}{c_m} \boldsymbol{d} \boldsymbol{N}^T \ , \tag{2}$$

in terms of the unknown homogenized fields $\boldsymbol{u}$ and $\boldsymbol{d}$

A careful averaging of the virtual work in the material micro-structure with respect to variations of variables $\boldsymbol{u}$ and $\boldsymbol{d}$, leads to the following expression:

$$\delta W = \ (c_m \boldsymbol{P}_m + c_f \boldsymbol{P}_f) : \nabla \delta \boldsymbol{u} + (\boldsymbol{P}_m - \boldsymbol{P}_f) : (\delta \boldsymbol{d} \ \boldsymbol{N}^T)$$
$$+ \frac{h_f^2}{12\, c_f} \mathcal{D} \boldsymbol{P}_f(\boldsymbol{F}_f) \left[\nabla \boldsymbol{d} \boldsymbol{T} \boldsymbol{T}^T \right] : \left(\nabla \delta \boldsymbol{d} \boldsymbol{T} \boldsymbol{T}^T \right) \ , \tag{3}$$

where c_f and $c_m = 1 - c_f$ are the volume fractions of the fiber and matrix respectively, $\boldsymbol{P}_f$ and $\boldsymbol{P}_m$ are the corresponding 1$^{\text{st}}$ Piola-Kirchhoff stress tensors, $\mathcal{D}\boldsymbol{P}_f$ is the directional derivative of the mapping $\boldsymbol{F}_f \mapsto \boldsymbol{P}_f$ and h_f is the fiber layer height. The first term in Eq. (3) expresses the classical force equilibrium and the second term expresses an internal equilibrium in the sense of the Reuss model. The last term corresponds to the part of the fiber bending energy that is not captured by the homogenized displacements field $\boldsymbol{u}$.

The 1$^{\text{st}}$ Piola-Kirchhoff stress tensors contained in Eq. (3) are based on hyper-elastic and hyper-elasto-plastic constitutive laws for the fiber and matrix materials respectively. Under consideration of Eqs. (1) and (2), these stress tensors can be written as closed form functions $\boldsymbol{P}_f(\nabla\boldsymbol{u}, \boldsymbol{d})$ and $\boldsymbol{P}_m(\nabla\boldsymbol{u}, \boldsymbol{d}, \xi_m)$ of the unknown variables and their gradients.

Eq. (3) is the basis of a corresponding finite-element formulation, which results to a discretized system with sufficient equations for solving for $\boldsymbol{u}$ and $\boldsymbol{d}$. One additional equation is necessary for solving for the plastic multiplier ξ_m. This is the plastic yield condition, expressed in weak form as

$$\int_{\Omega_0} r(\nabla\boldsymbol{u}, \boldsymbol{d}, \xi_m)\, \delta\xi_m \; dX = 0 \qquad \forall \;\; \delta\xi_m \;\; , \tag{4}$$

where Ω_0 is the considered solid domain in the undeformed configuration and $r(\nabla\boldsymbol{u}, \boldsymbol{d}, \xi_m)$ an appropriately chosen non-smooth complementarity function, which incorporates the plastic yield surface along with the corresponding Karush–Kuhn–Tucker conditions. A specific choice of the complementarity function r is provided in [10]. It should also be noted that the accumulated plastic strain in the matrix material γ_m at the current time instant depends on the corresponding value in the previous time instant and the unknown multiplier ξ_m for the current load step.

3. Numerical Examples

This section presents numerical results corresponding to two distinct examples under plane strain conditions. In the first example, a V-notched beam is subjected to pure bending load, until micro-buckling initiates at the notch tip due to the developed compressive stresses. The second example demonstrates micro-buckling initiation on the circumference of a circular void in a unidirectionally reinforced material, subjected to far-field longitudinal compression.

3.1. Bending of a V-notched beam

The geometry of the considered V-notched beam for this numerical example is defined through the overall beam height $H = 4.64$ mm and length $L = 20$ mm, the reduced beam height $H_0 = 3.867$ mm at the notch location, the notch opening angle $\theta = 67°$ and the notch tip radius $\rho = 0.196$ mm. All simulation results refer to a unit thickness, $t = 1$ mm. The beam is reinforced in its longitudinal direction with the reinforcing fiber layers exhibiting a sinusoidal misalignment in the region close to the notch tip. The wavelength of the misalignment is $p = 0.156$ mm and its amplitude $a = 0.52$ µm, resulting in a maximum misalignment angle of $0.6°$.

The reinforcement has an initial Young's modulus $E_f = 27600$ MPa and Poisson's ratio $\nu_f = 0.3$, while the corresponding elastic properties for the matrix material are $E_m = 1478.3$ MPa and $\nu_m = 0.38$. The matrix material is assumed to exhibit J$_2$-flow plastic behavior of Ramberg-Osgood type hardening, with the initial yield limit $\sigma_{ym} = 90$ MPa and parameters $n_m = 4$ and $\alpha_m = 3/7$. The fiber volume fraction is $c_f = 0.587$.

In order to determine the bending load capacity of the considered beam numerically, a prescribed bending angle at the beam ends is incremented by means of a numerical continuation procedure. The continuation procedure detects the critical load where a micro-buckling material instability initiates due to compressive stresses in the region close to the notch tip. Figure 2 shows snapshots of a 3.3 mm×1.8 mm region around the notch tip at the critical load for different values of the fiber height h_f.
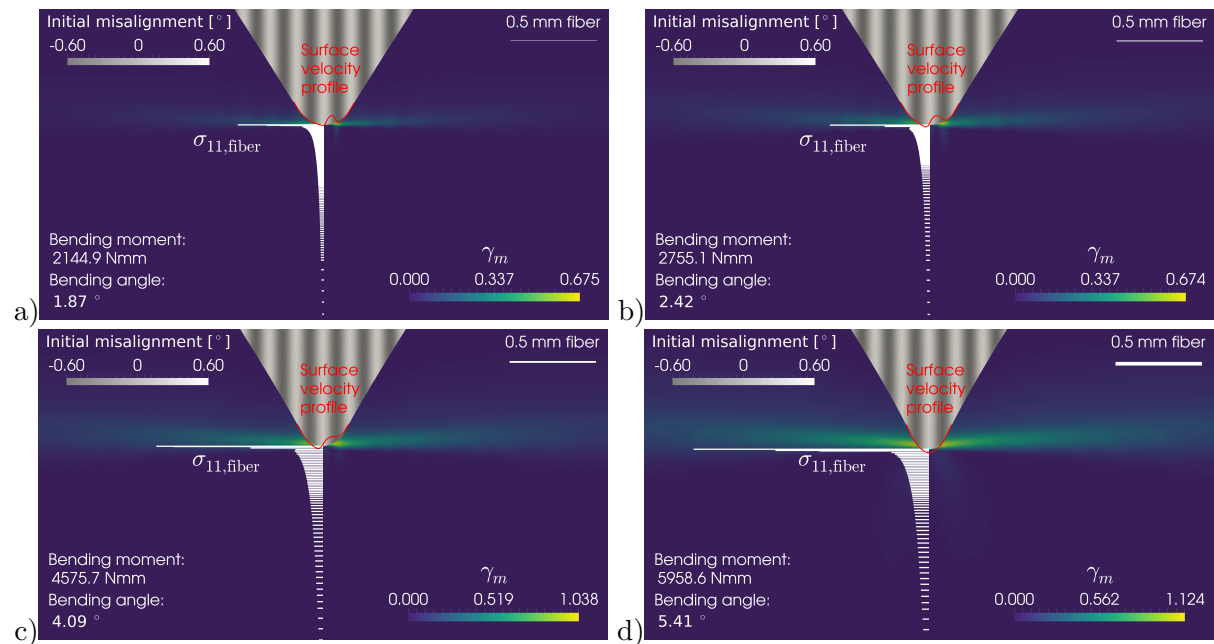
Figure 2. Snapshots of beam bending simulations at critical load for four different reinforcing fiber heights: a) 2.6 µm b) 5.2 µm c) 10.4 µm d) 20.8 µm.

The results presented in figure 2 make clear that the fiber height h_f has a large impact on the bending load capacity of the considered beam. In the case of the highest value of $h_f = 20.8$ µm, an almost triple bending angle and moment can be sustained compared to the case with the lowest $h_f = 2.6$ µm. The difference is also obvious in the longitudinal stress profiles on the cross-section through the notch, included in the snapshots. The micro-buckling modes for the four considered values of h_f are visualized through the surface velocity profile at the notch tip. The increased bending stiffness at higher beam heights results to smoothened velocity profiles and corresponding buckling modes. The color map in figure 2 illustrates the accumulated plastic strain in the matrix material γ_m, while the gray scale map in the background illustrates the variation of the fiber misalignment angle along the horizontal direction.
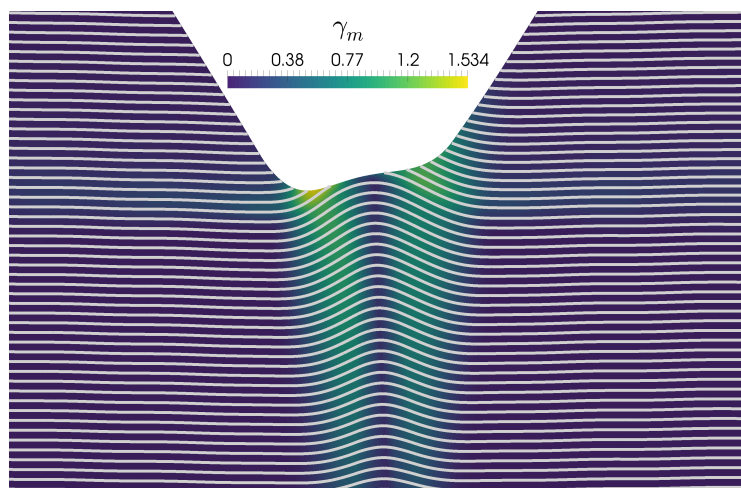

Figure 3. Snapshot of beam bending simulation in the post-buckling regime for reinforcing fiber height $h_f = 5.2$ µm.

For the case with $h_f = 5.2$ μm, figure 3 illustrates the deformed reinforcing fibers at approximately the same bending angle as the critical point shown in figure 2b, but posterior to the initiation of micro-buckling and the formation of a pair of kink-bands. The visualized streamlines were generated accounting for the direction of the deformed fibers but they are not supposed to capture the real density or thickness of the fiber layers.

3.2. Longitudinal compression of a specimen with a circular hole
The modeled geometry in the second numerical example corresponds to a circular disc of outer radius $R = 20$ mm with a concentric circular hole of radius $r = 1$ mm. The reinforcing material elasticity parameters are $E_f = 2.6 \cdot 10^5$ MPa and $G_f = 10^5$ MPa and the relevant matrix material parameters are $E_m = 2.6 \cdot 10^3$ MPa, $G_f = 10^3$ MPa, $\sigma_{ym} = 90$ MPa, $n_m = 4$ and $\alpha_m = 3/7$. As in the previous example, all presented results refer to a unit thickness $t = 1$ mm and plane strain conditions.

Far-field uniaxial compression is applied at the outer boundary with respect to the horizontal displacements, while two different load cases are considered regarding the vertical displacements, which are either constrained to zero or left free. The two cases are respectively referred to as transversely constrained ($\varepsilon_{22} = 0$) and transversely free ($\sigma_{22} = 0$).

The reinforcement is parallel to the horizontal direction and imperfection-free. Investigations with an imposed sinusoidal waviness imperfection of the reinforcement have shown that the effect of such imperfections is rather low, compared to the effect of the circular void itself and they are omitted here for the sake of simplicity.

Due to the available symmetries in the geometry, the reinforcement and the boundary conditions, it is sufficient to model only one quarter of the disc. Additional boundary conditions are necessary along the horizontal and vertical symmetry axes. The vertical and horizontal components of $\boldsymbol{u}$ are respectively fixed to zero along the two aforementioned axes and the horizontal component of $\boldsymbol{d}$ is fixed to zero on both symmetry axes.

As the far-field longitudinal strain ε_{11} is incremented within a numerical continuation scheme, a limit point is reached, where micro-buckling initiates near the top of the void circumference. Figure 4 shows snapshots corresponding to this limit point for two different values of the fiber height. Moreover the figure includes results both for the transversely constrained case, left from the vertical symmetry axis as well as for the transversely free case, right from the symmetry axis. The solid black line corresponds to the undeformed circumference, while the velocity profile on the void circumference is visualized by means of the red vectors.
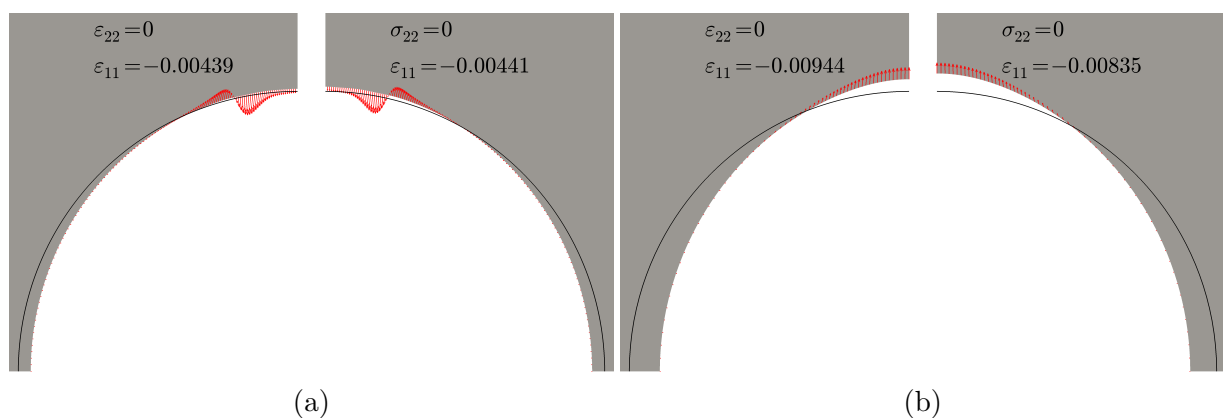

Figure 4. Snapshots at initiation of micro-buckling close to the circumference of a void in a longitudinal compressed reinforced composite for two different fiber heights: a) $h_f = 5$ μm and b) $h_f = 60$ μm.

For the highest value of h_f, micro-buckling initiates at a higher far-field strain, which is reflected in the considerably larger deformations observed in figure 4b. The critical far-field strain for the lowest value of h_f is approximately 0.44%, independent of the condition in the transverse direction. On the contrary, for the highest value of h_f, different critical strains are attained for the transversely constrained and transversely free cases, respectively equal to 0.94% and 0.84%.
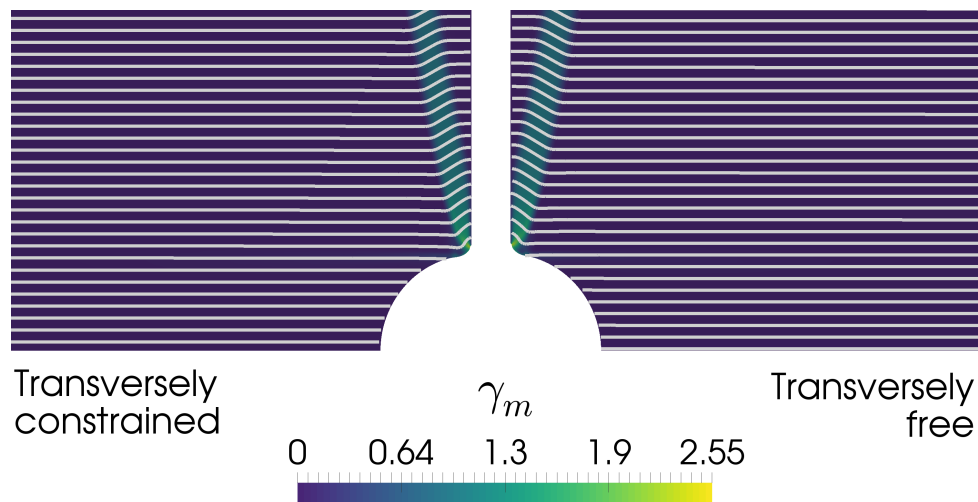

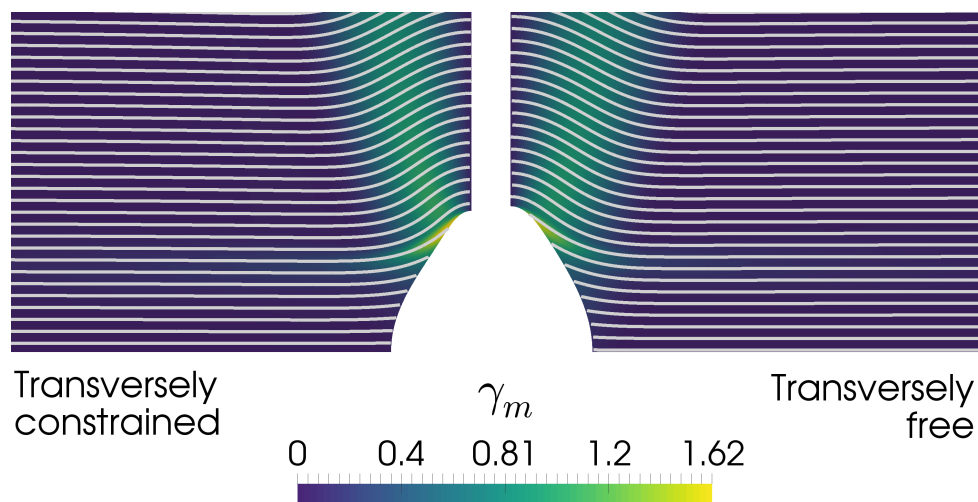**Figure 5.** Snapshot in the post-buckling regime for reinforcing fiber height $h_f = 5$ μm.

Figure 6. Snapshot in the post-buckling regime for reinforcing fiber height $h_f = 60$ μm.

Figures 5 and 6 show the post-buckling deformed solids in the region near the considered void, for the two different values of the fiber layer height, both for the transversely constrained and the transversely free cases. For the lowest fiber height value, the snapshots presented in figure 5 correspond to approximately the same far-field longitudinal strain as at the buckling initiation point shown in figure 4a, i.e. $\varepsilon_{11} = -0.0044$, but after the formation of the kink-bands that are visible in the region above the void. The differences between the two cases with respect to

the boundary condition in the transverse direction are minimal. Figure 6 shows corresponding snapshots in the post-buckling regime with regard to the highest fiber height value. It should be noted that the transversely free case shown in figure 6 is at a significantly lower far-field strain, $\varepsilon_{11} = -0.0084$, than the transversely constrained one, $\varepsilon_{11} = -0.0094$. Despite the lower applied strain, the observed deformations are similar, demonstrating the significant impact of the boundary condition in the transverse direction, for this example. Compared to figure 5, the formed kink-bands shown in figure 6 exhibit a significantly smoother transition, attributed to the higher bending stiffness of the fibers in this case.

4. Conclusions

The two numerical examples included in this work, demonstrate the crucial role of the fiber bending stiffness in predicting micro-buckling initiation in unidirectionally reinforced composite materials. At locations close to notches or holes, where significant stress gradients are present, compressive material instabilities were observed to initiate at very distinct levels of the maximum longitudinal compressive stress, depending on the assumed reinforcing fiber height. The numerical results show that the interplay between micro-structural effects and the overall geometry of the structure introduces a size scale effect which is not possible to capture by analytical models, unless a length scale parameter such as the reinforcing fiber layer height is considered.

Acknowledgments

References

[1] Fleck N 1997 *Adv. Appl. Mech.* **33** pp 43–117
[2] Rosen B W 1965 Mechanics of composite strengthening, in *Fibre Composite Materials* (Materials Park, OH: ASM) chap 3 pp 37–75
[3] Argon A S 1972 *Treatise on Materials Science and Technology* vol 1 pp 79–114
[4] Budiansky B 1983 *Comput. Struct.* **16** pp 3–12
[5] Budiansky B and Fleck N 1993 *J. Mech. Phys. Solids* **41** pp 183–211
[6] Waas A M, Babcock C and Knauss W 1990 *J. Appl. Mech.-T. ASME* **57** pp 138–149
[7] Fleck N and Shu J 1995 *J. Mech. Phys. Solids* **43** pp 1887–1918
[8] Kyriakides S, Perry E J and Liechti K M 1994 *Appl. Mech. Rev.* **47** pp S262–S268
[9] Wind J L, Waas A M and Jensen H M 2015 *Compos. Struct.* **122** pp 51–56
[10] Poulios K and Niordson C F 2016 *J. Mech. Phys. Solids* **94** pp 433–452